Composite Structures 161 (2017) 160–172

Contents lists available at ScienceDirect

Composite Structures

journal homepage: www.elsevier.com/locate/compstruct

Application of the inverse finite element method to design wind turbine blades

Alejandro Albanesi [a,*], Victor Fachinotti [a], Ignacio Peralta [a], Bruno Storti [a], Cristian Gebhardt [b]

[a] CIMEC Centro de Investigación de Métodos Computacionales, UNL, CONICET Col. Ruta 168 s/n, Predio Conicet Dr Alberto Cassano, 3000 Santa Fe, Argentina
[b] Institut für Statik und Dynamik, Leibniz Universität Hannover, Appelstraße 9A, 30167 Hannover, Germany

ARTICLE INFO

Article history:
Received 1 September 2016
Revised 1 November 2016
Accepted 11 November 2016
Available online 16 November 2016

Keywords:
Wind turbine blade
Inverse finite element
Large elastic deformation
Degenerated solid shell
Multilayered shell
Composite layer

ABSTRACT

This paper presents a novel methodology to design wind turbine blades using the Inverse Finite Element Method (IFEM). IFEM takes as domain of analysis the geometry of the blade after large elastic deformations caused by given service loads. The deformed shape of the blade is that determined to be efficient using an aerodynamics analysis. From this analysis, the aerodynamic loads on the blade are known.

Then, we choose the materials to manufacture the blade. As usual, the blade is assumed to be made of multiple layers of composite materials. After materials selection, the stationary inertial loads on the blade are known.

Finally, given the desired deformed shape and all the service loads, we use IFEM to compute the manufacturing shape of the blade. This is a one-step, one-direction strategy where the aerodynamics analysis feeds the structural (IFEM) analysis, and no further interaction between both solvers is required.

As an application of the proposed strategy, we consider a medium power 40-KW wind turbine blade, whose whole design is detailed along this work.

1. Introduction

Energy is a vital element for the economic growth of most countries. The rising concern about climate change and pollution has led to the development and improvement of renewable energy sources. Wind energy is the fastest-growing renewable source, and the World Energy Council (WEC) [1] has predicted that it will continue its expansion in any of the given policy scenarios to the year 2050. The most common device to convert the kinetic energy of the wind into electrical power is the horizontal axis wind turbine (HAWT), typically having a three-blade rotor, the so-called Danish concept.

This work introduces the design of the blade of a HAWT such that it attains a desired shape under service loads. The so-called desired shape is the aerodynamically efficient shape of the blade determined from an aerodynamic analysis. A wind turbine blade is usually a compliant, slender, shell-like structure that undergoes large displacements and rotations as result of aerodynamic and stationary inertial forces. These large deformations must lie in the elastic range, which is usually ensured by manufacturing the blade of several layers of composite materials. The choice of such materials is favored by plenty of reasons, including their excellent strength-to-weight ratio, flexibility to fit complicated shapes, good fatigue properties [2], resistance to oils and lubricants [3], and dimensional stability under different environmental conditions [4,5]. Once the number of layers, their thickness and material are defined, the stationary inertial forces on the blade are completely determined.

Known the desired deformed geometry, the materials, and the service loads (aerodynamic and stationary inertial forces), the manufacturing shape of the blade has to be determined, Fig. 1.

Bazilevs et al. [6] accomplished this task by solving a sequence of non-linear equilibrium equations posed on this unknown configuration. At each step, given an undeformed configuration (coincident to the known deformed configuration in the first step), the displacement solution of the equilibrium equation serves to update the undeformed configuration for the next step, process that is repeated until convergence. In that work, those authors modeled the blade using the isogeometric rotation-free Kirchhoff–Love shell formulation [7](see Fig. 2).

The undeformed configuration of a body can be also determined by solving a nonlinear optimization problem where the closeness to the desired deformed configuration is the cost function to be minimized. This is done by Chen et al. [8], who proposed the asymptotic numerical method. This is a multistep iterative method

* Corresponding author.
E-mail address: aalbanesi@cimec.santafe-conicet.gov.ar (A. Albanesi).

http://dx.doi.org/10.1016/j.compstruct.2016.11.039
0263-8223/

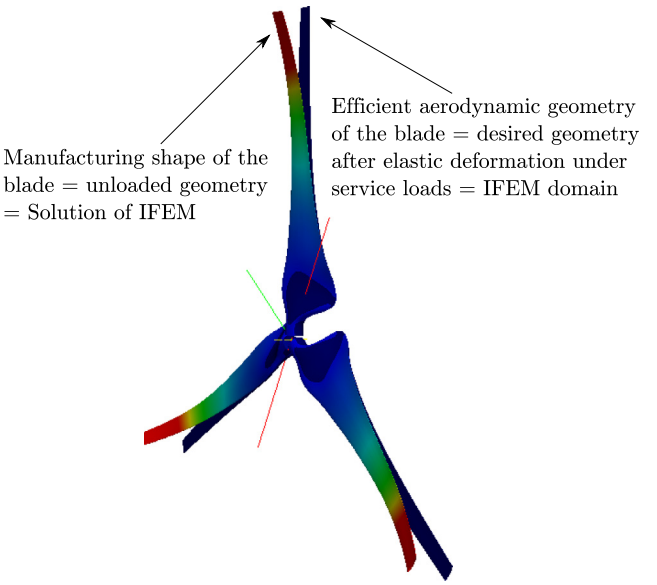

Fig. 1. Inverse analysis of wind turbine blades: the efficient aerodynamic geometry of the blade (in solid color) is the domain of IFEM. The manufacturing shape of the blade (in color gradient) is the IFEM solution.

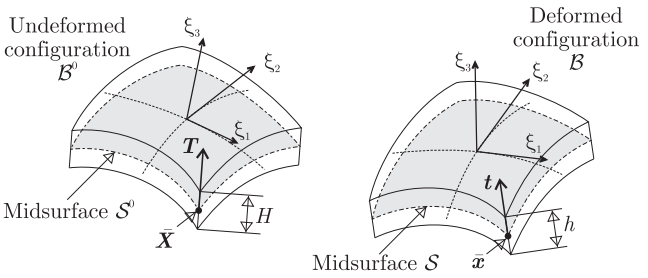

Fig. 2. Geometric representation of the undeformed and deformed configurations of a shell.

where the equilibrium equation has to be solved at each iteration of each step.

A third approach for the computation of the undeformed configuration of a body is the Inverse Finite Element Method (IFEM) [9–11]. IFEM solves the equilibrium equation in the deformed configuration to obtain the undeformed shape. Unlike the just mentioned multistep strategies, IFEM solves a nonlinear equilibrium equation only once. Fachinotti et al. [9] applied IFEM to the design of an aircraft turbine blade using three-dimensional solid finite elements. This model is capable of handling anisotropic materials and could be used in this case. But to model a turbine blade using standard solid elements is an expensive choice. Later, IFEM was extended to shell finite elements [11] and applied to the design of shell structures made of one transversely isotropic layer. This model is based on the Mindlin-Reissner shell theory, so that it takes into account the transverse shear deformation and henceforth is capable of representing thin to moderately thick shells unlike the models based on the Kirchhoff–Love theory.

In this work, we supply this shell element with the capability of representing shells made of multiple layers of transversely orthotropic materials, in order to apply it to the design of wind turbine blades. The implementation of the proposed element is validated against a benchmark, and two numerical examples with different composite material layout demonstrate the capabilities and potentialities of the current inverse approach.

This paper is organized as follows: Section 2 presents a brief overview of the non-linear shell IFEM, a step by step procedure used to compute the manufacturing shape of the blade, and a feasibility criteria to verify the IFEM solution. Section 3 is concerned with the input data required for IFEM, and consists in the design of an efficient aerodynamic shape of the blade, the computation of the aerodynamic loads with Computational Fluid Dynamics (CFD), the creation of a shell finite element mesh of the blade surface, the transfer of data from CFD to the IFEM mesh, and the selection of proper composite materials. Section 4 includes a validation benchmark for the multilayer shell IFEM, and the solution of two numerical examples. The concluding remarks are given in Section 5. Appendix A includes further information on the aerodynamic analysis, and a validation benchmark for CFD.

2. IFEM model and procedure

This section introduces the IFEM shell model, and describes the procedure to compute the manufacturing shape of a the multilayer wind turbine blade such that it attains the prescribed aerodynamic configuration under service loads.

2.1. Inverse shell finite element model

Up to this point, the desired aerodynamic shape of the blade, say $\mathcal{B}^0$, as well as the loads that should deform the blade to this shape, are known. The goal then is to compute the unloaded configuration of the blade, say $\mathcal{B}$, that dictates how to fabricate the blade such that it attains the desired shape under the given loads. For the case of blades, which are shell-like structures, let us use the IFEM for shells [11]. For the sake of completeness, a self-contained summary of such method is given in this section.

2.1.1. Shell kinematics and deformation

Using shell kinematics, the position of any point $\boldsymbol{X} \in \mathcal{B}^0$ is expressed as follows:

$$\boldsymbol{X}(\xi_1,\xi_2,\xi_3) = \bar{\boldsymbol{X}}(\xi_1,\xi_2) + \xi_3 \frac{H}{2}\boldsymbol{T}(\xi_1,\xi_2), \tag{1}$$

where $\bar{\boldsymbol{X}}$ lies in the midsurface $\mathcal{S}^0$ of $\mathcal{B}^0$, $\boldsymbol{T}$ is the material director vector, H is the thickness, and $\{\xi_1,\xi_2,\xi_3\}$ is a system of natural coordinates with origin $\bar{\boldsymbol{X}}$, such that ξ_1 and ξ_2 lie in $\mathcal{S}^0$.

Let $\mathcal{B}$ be the deformed configuration of the shell, with midsurface $\mathcal{S}$. After deformation, the point $\boldsymbol{X} \in \mathcal{B}^0$ occupies the position $\boldsymbol{x} \in \mathcal{B}$:

$$\boldsymbol{x}(\xi_1,\xi_2,\xi_3) = \bar{\boldsymbol{x}}(\xi_1,\xi_2) + \xi_3 \frac{h}{2}\boldsymbol{t}(\xi_1,\xi_2), \tag{2}$$

where $\bar{\boldsymbol{x}} \in \mathcal{S}, \boldsymbol{t}$ is the unit vector known as spatial director, and $h = h(\xi_1,\xi_2)$ is the thickness of the deformed shell.

We further adopt the Mindlin-Reissner plate theory, which allows $\boldsymbol{t}$ not being normal to $\mathcal{S}$ if $\boldsymbol{T}$ is normal to $\mathcal{S}^0$ (and vice versa) as an effect of shear deformation, and assumes that the strain normal to the mid-surface is null, so $h = H$.

Inside a generic isoparametric finite element, $\boldsymbol{x} \in \mathcal{B}$ and $\boldsymbol{X} \in \mathcal{B}^0$ are interpolated as follows:

$$\boldsymbol{X}(\xi_1,\xi_2,\xi_3) = \varphi_i\left[\bar{\boldsymbol{X}}_i + \frac{\xi_3}{2}h\boldsymbol{T}_i\right] = \boldsymbol{\Phi}(\xi_1,\xi_2,\xi_3)\boldsymbol{Q}, \tag{3}$$

$$\boldsymbol{x}(\xi_1,\xi_2,\xi_3) = \varphi_i\left[\bar{\boldsymbol{x}}_i + \frac{\xi_3}{2}h\boldsymbol{t}_i\right] = \boldsymbol{\Phi}(\xi_1,\xi_2,\xi_3)\boldsymbol{q}, \tag{4}$$

with

$$\boldsymbol{\Phi} = \left[\varphi_1\boldsymbol{I} \quad \tfrac{\xi_3}{2}h\varphi_1\boldsymbol{I} \quad \cdots \quad \varphi_N\boldsymbol{I} \quad \tfrac{\xi_3}{2}h\varphi_N\boldsymbol{I}\right], \tag{5}$$

$$\boldsymbol{Q}=\begin{bmatrix}\bar{\boldsymbol{X}}_1\\ \boldsymbol{T}_1\\ \vdots\\ \bar{\boldsymbol{X}}_N\\ \boldsymbol{T}_N\end{bmatrix},\qquad \boldsymbol{q}=\begin{bmatrix}\bar{\boldsymbol{x}}_1\\ \boldsymbol{t}_1\\ \vdots\\ \bar{\boldsymbol{x}}_N\\ \boldsymbol{t}_N\end{bmatrix}, \tag{6}$$

where $(\bar{\boldsymbol{X}}_i,\boldsymbol{T}_i)$ defines the position of the node $i=1,2,\dots N$ of the undeformed finite element, $(\bar{\boldsymbol{x}}_i,\boldsymbol{t}_i)$ defines the position of the node i of the deformed finite element, and $\varphi_i=\varphi_i(\xi_1,\xi_2)$ is the 2-D shape function associated to node i; $\boldsymbol{I}$ is the 3×3-identity matrix.

Then, the deformation of the shell is measured using the Green–Lagrange strain tensor defined as

$$\boldsymbol{E}=\underbrace{\frac{1}{2}(\boldsymbol{g}_\alpha\cdot\boldsymbol{g}_\beta-\boldsymbol{G}_\alpha\cdot\boldsymbol{G}_\beta)}_{E^{\mathrm{cov}}_{\alpha\beta}}\boldsymbol{G}^\alpha\otimes\boldsymbol{G}^\beta, \tag{7}$$

where $E^{\mathrm{cov}}_{\alpha\beta}$ are the so-called covariant components of $\boldsymbol{E}$, $\boldsymbol{g}_\alpha=\partial\boldsymbol{x}/\partial\xi_\alpha$ and $\boldsymbol{G}_\alpha=\partial\boldsymbol{X}/\partial\xi_\alpha$ are the spatial and convective basis vectors, respectively, and $\boldsymbol{G}^\alpha$ is a vector of the contravariant base reciprocal to $\{\boldsymbol{G}_\alpha\}$ (i.e., $\boldsymbol{G}^\alpha\cdot\boldsymbol{G}_\beta$ equals either 0 for $\alpha\neq\beta$ or 1 for $\alpha=\beta$). Using FEM, it yields

$$E^{\mathrm{cov}}_{\alpha\beta}=\frac{1}{2}\left(\boldsymbol{q}^T\boldsymbol{A}_{\alpha\beta}\boldsymbol{q}-\boldsymbol{Q}^T\boldsymbol{A}_{\alpha\beta}\boldsymbol{Q}\right), \tag{8}$$

where $\boldsymbol{A}_{\alpha\beta}$ is the $6N\times 6N$-symmetric matrix defined by

$$\boldsymbol{A}_{\alpha\beta}=\frac{1}{2}\left(\frac{\partial\boldsymbol{\Phi}^T}{\partial\xi_\alpha}\frac{\partial\boldsymbol{\Phi}}{\partial\xi_\beta}+\frac{\partial\boldsymbol{\Phi}^T}{\partial\xi_\beta}\frac{\partial\boldsymbol{\Phi}}{\partial\xi_\alpha}\right). \tag{9}$$

Cure for shear locking. The stiffness of low-order finite elements increases spuriously as the ratio thickness/in-plane dimension of the element decreases. This is the well-known "shear locking" problem, which affects even cubic order elements.

One of the simpler cures for "shear locking" is the use of the "assumed-strain" technique. In particular, we use the MITC4 formulation, initially proposed by Dvorkin and Bathe [12].

The MITC4 finite element is a quadrangle with nodes located at its vertices, and bilinear shape functions ϕ_i. Inside this element, the covariant strain fields E^{cov}_{ij} are defined by Eq. (8), except the fields E^{cov}_{13} and E^{cov}_{23} that are replaced by the respective "assumed" strain fields:

$$\tilde{E}^{\mathrm{cov}}_{13}(\xi_2,\xi_3)\approx\frac{1+\xi_2}{2}E^{\mathrm{cov}}_{13}(0,1,\xi_3)+\frac{1-\xi_2}{2}E^{\mathrm{cov}}_{13}(0,-1,\xi_3), \tag{10}$$

$$\tilde{E}^{\mathrm{cov}}_{23}(\xi_1,\xi_3)\approx\frac{1+\xi_1}{2}E^{\mathrm{cov}}_{23}(1,0,\xi_3)+\frac{1-\xi_1}{2}E^{\mathrm{cov}}_{23}(-1,0,\xi_3) \tag{11}$$

This amounts to replace matrices $\boldsymbol{A}_{\alpha\beta}$ for $\alpha\beta=13,23$ in Eq. (8) by

$$\tilde{\boldsymbol{A}}_{13}(\xi_2,\xi_3)\approx\frac{1+\xi_2}{2}\boldsymbol{A}_{13}(0,1,\xi_3)+\frac{1-\xi_2}{2}\boldsymbol{A}_{13}(0,-1,\xi_3), \tag{12}$$

$$\tilde{\boldsymbol{A}}_{23}(\xi_1,\xi_3)\approx\frac{1+\xi_1}{2}\boldsymbol{A}_{23}(1,0,\xi_3)+\frac{1-\xi_1}{2}\boldsymbol{A}_{23}(-1,0,\xi_3). \tag{13}$$

From now on, for $\alpha\beta=13,23$, "direct" $E^{\mathrm{cov}}_{\alpha\beta}$ and $\boldsymbol{A}_{\alpha\beta}$ are replaced by "assumed" $\tilde{E}^{\mathrm{cov}}_{\alpha\beta}$ and $\tilde{\boldsymbol{A}}_{\alpha\beta}$ respectively, and the superimposed tilde that identifies the assumed quantities will be obviated in order to simplify the notation.

2.1.2. Equilibrium equations for shells using FEM

The equilibrium of shells, when modeled as degenerated solids, is governed by the same variational principle governing the equilibrium of general solids, whose Lagrangian formulation can be written as:

$$\int_{\mathcal{B}^0}S^{\alpha\beta}\delta E_{\alpha\beta}\,\mathrm{d}V=\mathcal{W}^{\mathrm{ext}}(\delta\boldsymbol{u}), \tag{14}$$

for all admissible variation of the displacement $\boldsymbol{u}$, where $S^{\alpha\beta}$ are the contravariant components of the second Piola–Kirchhoff stress tensor $\boldsymbol{S}$ (work-conjugate to $\boldsymbol{E}$), $\delta E_{\alpha\beta}$ are the variations of the covariant components of $\boldsymbol{E}$, and $\mathcal{W}^{\mathrm{ext}}$ is the work of the external forces (surface tractions and body forces) on the whole body under a displacement $\delta\boldsymbol{u}$. For an elastic solid, the constitutive equation for $\boldsymbol{S}$ can be generally expressed as a function of $\boldsymbol{E}$:

$$\boldsymbol{S}=\boldsymbol{S}(\boldsymbol{E}). \tag{15}$$

Let us recall that, following the Mindlin-Reissner plate theory, the normal stress in the direction normal to the midsurface (that of $\boldsymbol{G}^3$) is assumed to be zero [13].

Regarding the displacement variation, it can be written for "direct" FEM as follows:

$$\delta\boldsymbol{u}=\delta\boldsymbol{x}=\boldsymbol{\Phi}\delta\boldsymbol{q}. \tag{16}$$

Being $\delta\boldsymbol{q}$ made of nodal $\delta\bar{\boldsymbol{x}}_i$ and $\delta\boldsymbol{t}_i$, the latter deserves a special treatment in order to account for the inextensibility of the director vector. Following Simo et al. [14], the increment of $\boldsymbol{t}_i$ is as follows:

$$\delta t_i=\tilde{\boldsymbol{\lambda}}_i\delta\tilde{t}_i\qquad(\text{no summation over } i,) \tag{17}$$

where $\delta\tilde{t}_i$ is a vector lying in the plane $\{i,j\}$ of the fixed global Cartesian frame $\{i,j,k\}$, and $\tilde{\boldsymbol{\lambda}}_i$ is the 3×2-matrix made of the first two columns of the orthogonal matrix $\boldsymbol{\lambda}_i$ from the transformation

$$t_i=\boldsymbol{\lambda}_i k. \tag{18}$$

Being $k=[0,0,1]^T$ fixed, the above equation defines $\boldsymbol{\lambda}_i$ as a function of t_i.

Further details on the current implementation of the nodal director update are given in our original work on IFEM for shells [11]. For the purpose of the current discussion, let us just notice that Eq. (17) involves only two degrees of freedom to update the nodal director, making the current formulation have five degrees of freedom per node. Consequently, δq is replaced by

$$\delta q=\underbrace{\begin{bmatrix}\boldsymbol{I}&\tilde{\boldsymbol{0}}&\cdots&\boldsymbol{0}&\tilde{\boldsymbol{0}}\\ \boldsymbol{0}&\tilde{\boldsymbol{\lambda}}_1&\cdots&\boldsymbol{0}&\tilde{\boldsymbol{0}}\\ \vdots&\vdots&\ddots&\vdots&\vdots\\ \boldsymbol{0}&\tilde{\boldsymbol{0}}&\cdots&\boldsymbol{I}&\tilde{\boldsymbol{0}}\\ \boldsymbol{0}&\tilde{\boldsymbol{0}}&\cdots&\boldsymbol{0}&\tilde{\boldsymbol{\lambda}}_N\end{bmatrix}}_{\boldsymbol{\Lambda}(q)}\underbrace{\begin{bmatrix}\delta\bar{\boldsymbol{x}}_1\\ \delta\tilde{t}_1\\ \vdots\\ \delta\bar{\boldsymbol{x}}_N\\ \delta\tilde{t}_N\end{bmatrix}}_{\delta\tilde{q}}, \tag{19}$$

where $\boldsymbol{0}$ and $\tilde{\boldsymbol{0}}$ denote the 3×3- and 3×2-zero matrices, respectively, and the dependence of $\boldsymbol{\Lambda}$ on q can be inferred from Eq. (18).

Now, the variation of the covariant strains (given by Eq. (8)) is

$$\delta E_{\alpha\beta}=\delta q^T A_{\alpha\beta}q^T=\delta\tilde{q}^T\boldsymbol{\Lambda}^T A_{\alpha\beta}q^T \tag{20}$$

Using the above expression for $\delta E_{\alpha\beta}$, the l.h.s. of Eq. (14) takes the form

$$\begin{aligned}\int_{\mathcal{B}^0}S^{\alpha\beta}\delta E_{\alpha\beta}\,\mathrm{d}V&=\delta q^T\mathbf{F}^{\mathrm{int}}(q,Q)\\&=\delta\tilde{q}^T\underbrace{[\boldsymbol{\Lambda}(q)]^T\mathbf{F}^{\mathrm{int}}(q,Q)}_{\tilde{\mathbf{F}}^{\mathrm{int}}(q,Q)},\end{aligned} \tag{21}$$

where it is introduced the vector of nodal internal loads:

$$\mathbf{F}^{\mathrm{int}}(q,Q)=\int_{\mathcal{B}^0(Q)}S^{\alpha\beta}(q,Q)A_{\alpha\beta}q^T\,\mathrm{d}V. \tag{22}$$

The dependence of $S^{\alpha\beta}$ on q and Q becomes evident by introducing E as a function of Q and q (as given by Eqs. (7) and (8)) into the constitutive Eq. (15).

Analogously, assuming the external loads to be lumped at the nodes and grouped in the vector $\mathbf{F}^{\text{ext}}$, the r.h.s. of Eq. (14) can be written as

$$\begin{aligned}\mathcal{W}^{\text{ext}}(q,Q) &= \delta q^T \mathbf{F}^{\text{ext}}(q,Q) \\ &= \delta\tilde{q}^T \underbrace{[\boldsymbol{\Lambda}(q)]^T \mathbf{F}^{\text{ext}}(q,Q)}_{\tilde{\mathbf{F}}^{\text{ext}}(q,Q)},\end{aligned} \tag{23}$$

where it is admitted that the external forces generally depends on Q (body forces are usually given by unit undeformed volume) and q (as in the case of wind pressure).

Finally, by introducing Eqs. (21) and (23) in the variational principle (14) for arbitrary $\delta\tilde{q}$, we obtain

$$\tilde{\mathbf{R}}(q,Q) = \tilde{\mathbf{F}}^{\text{int}}(q,Q) - \tilde{\mathbf{F}}^{\text{ext}}(q,Q) = \mathbf{0}. \tag{24}$$

that is the equilibrium equation for "direct" FEM applied to degenerated-solid shells, which is a nonlinear equation for the unknown q, with Q given.

2.1.3. Equilibrium equations for shells using IFEM

In inverse finite element analysis, the loaded configuration B, as well as the external loads responsible of deforming the shell from B^0 to B, are assumed to be known. In our previous works [9,10], we chose to formulate the variational principle (14) using Eulerian stress and strain measures. However, we use a different approach for shells [11] to highlight the close relationship between FEM and IFEM: both have the identical governing equation, that given by the discrete equilibrium Eq. (24), differing only in the fact that knowns and unknowns are interchanged.

Then, Eq. (24) defines also the equilibrium equation for IFEM applied to degenerated-solid shells, being now a nonlinear equation for the unknown Q for a given q. This is a nonlinear equation to be solved using the Newton–Raphson method: at the iteration $k+1, Q$ is updated by solving the linear equation for $\delta\tilde{Q}$:

$$\tilde{\mathbf{R}}(q,Q^{(k+1)}) = \tilde{\mathbf{R}}(q,Q^{(k)}) + \left.\frac{\partial\tilde{\mathbf{R}}}{\partial\tilde{Q}}\right|_{Q^{(k)}} \Delta\tilde{Q} = \mathbf{0}. \tag{25}$$

where $\partial\tilde{\mathbf{R}}/\partial\tilde{Q}$ is the tangent stiffness matrix (see [11] for details), and

$$\Delta\tilde{Q} = \begin{bmatrix} \Delta\bar{X}_1 \\ \Delta\tilde{T}_1 \\ \vdots \\ \Delta\bar{X}_N \\ \Delta\tilde{T}^*_N \end{bmatrix} \tag{26}$$

Once $\Delta\tilde{Q}$ is computed, the nodal position $\bar{X}_i \in \mathcal{S}^0$ is straightforwardly updated:

$$\bar{X}_i^{(k+1)} = \bar{X}_i^{(k)} + \Delta\bar{X}_i. \tag{27}$$

2.1.4. Update of the material director vector

However, the update of the nodal material director $T_i \in \mathbb{R}^3$ from $\Delta\tilde{T}_i \in \mathbb{R}^2$ deserves a special treatment. We proceed here in a way identical to that proposed by Simo et al. [14] for the "direct" shell FEM. Starting from the given initial guess $T_i^{(0)}$, we compute the orthogonal rotation matrix

$$\boldsymbol{\chi}_i^{(0)} = (k\cdot T_i^{(0)})I + k\times\widehat{T_i^{(0)}} + \frac{(k\times T_i^{(0)})\otimes(k\times T_i^{(0)})}{1+k\cdot T_i^{(0)}}, \tag{28}$$

where $\widehat{v}$ is the skew-symmetric matrix whose axial vector is v. Usually, $T_i^{(0)} \equiv t_i$ and, in such a case, $\boldsymbol{\chi}_i^{(0)} \equiv \boldsymbol{\lambda}_i$ is the matrix of Eq. (18).

Known T_i and $\boldsymbol{\chi}_i$ at iteration k, they are updated using $\Delta\tilde{T}_i$ (solution of Eq. (25) at iteration $k+1$) following the next steps:

i) Compute

$$\Delta T_i = \tilde{\boldsymbol{\chi}}_i^{(k)} \Delta\tilde{T}_i, \tag{29}$$

where $\tilde{\boldsymbol{\chi}}_i^{(k)}$ is the 3×2-matrix made of the first two columns of $\boldsymbol{\chi}_i^{(k)}$.

ii) Update T_i:

$$T_i^{(k+1)} = \cos\|\Delta T_i\| T_i^{(k)} + \frac{\sin\|\Delta T_i\|}{\|\Delta T_i\|}\Delta T_i, \tag{30}$$

iii) Update $\boldsymbol{\chi}_i$:

$$\boldsymbol{\chi}_i^{(k+1)} = \Delta\boldsymbol{\chi}_i \boldsymbol{\chi}_i^{(k)}, \tag{31}$$

with

$$\begin{aligned}\Delta\boldsymbol{\chi}_i = \cos\|\Delta T_i\| I_{3\times 3} + \frac{\sin\|\Delta T_i\|}{\|\Delta T_i\|}\widehat{T_i^{(k)}\times\Delta T_i} + \frac{1-\cos\|\Delta T_i\|}{\|\Delta T_i\|^2} \\ \times (T_i^{(k)}\times\Delta T_i)\otimes(T_i^{(k)}\times\Delta T_i).\end{aligned} \tag{32}$$

The iterative process of solving Eq. (25) and updating X_i and T_i is repeated until $\|\tilde{\mathbf{R}}(q,Q^{(k+1)})\|$ is close enough to zero.

2.1.5. Integration for multilayer shell finite elements

At each shell finite elements, we have to compute integrals like that defining the vector of internal loads, Eq. (22), generically written as

$$\int_{\mathcal{B}^0} F(\xi_1,\xi_2,\xi_3)\,\mathrm{d}V. \tag{33}$$

First, since $\mathcal{B}$ is the known domain for IFEM, let us make the following change in the integration domain:

$$\int_{\mathcal{B}^0} F(\xi_1,\xi_2,\xi_3)\,\mathrm{d}V = \int_{\mathcal{B}} f(\xi_1,\xi_2,\xi_3)\,\mathrm{d}v, \tag{34}$$

with

$$f = FJ^{-1}, \tag{35}$$

where J is the Jacobian determinant of the transformation from $\mathcal{B}^0$ to $\mathcal{B}$, given by

$$J = \frac{\mathrm{d}v}{\mathrm{d}V} = \frac{(g_1\times g_2)\cdot g_3}{(G_1\times G_2)\cdot G_3}. \tag{36}$$

Then, as it a common practice for shells, the integral on $\mathcal{B}$ with mid-surface $\mathcal{S}$ is computed as

$$\int_{\mathcal{B}} f\,\mathrm{d}v = \int_{-1}^{1}\frac{h}{2}\int_{\mathcal{S}} f\,\mathrm{d}s\,\mathrm{d}\zeta, \tag{37}$$

where $\zeta \equiv \xi_3$ is the natural coordinate across the thickness of the shell.

Let the shell be made of n layers, and be h_i the thickness of layer i, such that $h = \sum h_i$. The points in the layer i are those with natural coordinates $\zeta \in (\zeta_{i-1},\zeta_i)$, with $\zeta_0 = -1, \zeta_n = 1$ and $\zeta_i = \zeta_{i-1} + 2h_i/h$. Then, the integral (37) is computed as

$$\int_{\mathcal{B}} f\,\mathrm{d}v = \sum_{i=1}^{n}\int_{\zeta_{i-1}}^{\zeta_i}\frac{h}{2}\int_{\mathcal{S}} f\,\mathrm{d}s\,\mathrm{d}\zeta. \tag{38}$$

The line and area integrals involved in the above equations are numerically computed using Gauss quadrature. Using MITC4 elements, following the pioneering work of Dvorkin and Bathe [12], a 2×2-point rule is used for the area integral, and a 2-point rule is used for the line integral. In the case of a multilayered shell, 2 points are utilized for the line integral over each layer.

2.2. Inverse design procedure

The procedure to compute the manufacturing shape of the blade with IFEM is summarized in the following steps, and is depicted in the flowchart of Fig. 3.

a) The efficient geometry of the wind turbine blade at a given operation condition is defined by a proper set of airfoils, and by the use of an appropriate chord and twist distribution. If the geometry of the blade is already prescribed, the designer should skip this step.
b) The blade is discretized with an unstructured tetrahedral mesh to perform the CFD analysis at the prescribed operation condition. The resultant aerodynamic forces at the nodes of this unstructured mesh in the three axis directions (X, Y, and Z) are computed.

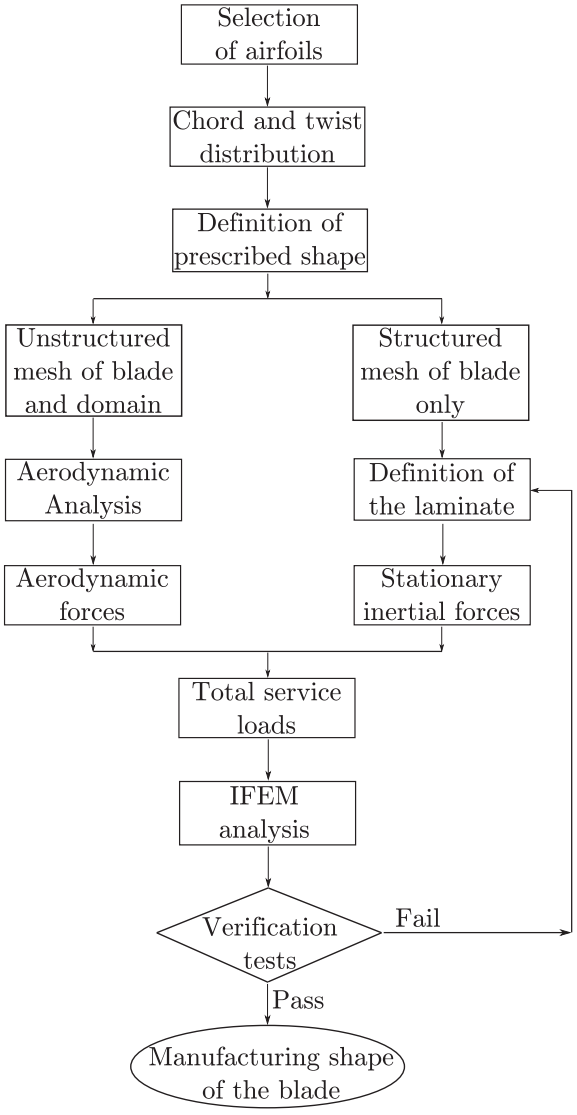

Fig. 3. Flowchart of the procedure to compute the manufacturing shape of the blade with IFEM.

c) For the IFEM analysis, the surface of the blade is discretized into a structured quadrilateral mesh. Refinement is used in curved areas such as the leading edge and trailing edge of the blade. This mesh is the desired geometry after elastic deformation and constitutes the IFEM domain.
d) The mechanical properties of the composite material are configured. The elastic modulus in each direction, fiber order and orientation, Poisson ratio, density, thickness, and ply drop configuration are defined.
e) The stationary inertial forces about the rotation axis are computed in each finite element of the quadrilateral mesh of *step c*, considering density and thickness of the composite, turbine rotational velocity, and distance to the rotation axis. Elemental forces are transformed in nodal forces.
f) The resultant aerodynamic forces at the nodes of the unstructured discretization of *step b*, are projected on the nodes of the structured discretization of *step c*. This projection is verified by comparison of the net force on the blade along the three axis directions (X, Y, and Z), and by comparison of force distribution over the surface in each mesh.
g) The total nodal forces over the blade are computed by adding the nodal stationary inertial forces of *step e* with the nodal aerodynamic forces of *step f*. These total forces are known data in the IFEM analysis.
h) Given the prescribed aerodynamic geometry of *step a* and the total forces of *step g* as known data, IFEM computes the manufacturing shape of the wind turbine blade.
i) The solution of IFEM must be verified using topological, mechanical, and numerical tests. More details on these tests are presented below.
j) If all the verification tests of *step i* are successful, the solution of IFEM computed at *step h* will attain the desired prescribed geometry of *step a*, when it is subjected to service loads computed at *step g*.

2.3. Verification of the IFEM solution

The solution computed with IFEM must pass a series of test that assures the feasibility of the solution, as detailed by Albanesi et al. [15,16]. These tests consists in the verification of:

1. *Inter-penetrated elements*: Concerning the topology, in some cases IFEM may lead to a useless solution containing inter-penetrated or intercrossed elements. This verification is performed to the nodal coordinates and connectivity of the solution.
2. *Validity of the hypothesis of elasticity*: the maximal stress in each material of the laminate must be lower than the yield strength.
3. *Uniqueness of the solution*, which is lost when an unstable equilibrium state (or critical point) is met during deformation. The uniqueness can be formally confirmed by using the spectrum test [17,18] and becomes evident for an experienced designer.

3. Description of IFEM input data

3.1. Efficient aerodynamic shape and aerodynamic forces

This subsection covers the determination of an efficient shape for the blades of a medium power, 40 KW three-blade HAWT to operate in the suburban area of Santa Fe city, Argentina (latitude 31 °38′S, longitude 60°42′W, mean altitude 25 m.a.s.l.). The turbine radius was chosen to be R = 6.70 m, and the prescribed operation conditions are considered to be wind velocity of 7 m/s and rotational velocity of 72 RPM. An efficient aerodynamic shape is determined by the selection of airfoils, and by using an appropriate law for chord and twist distribution. The resultant aerodynamic

forces due to pressure gradients and viscous flow, and the torque produced by the blades, have been determined using the steady-state solver for incompressible turbulent flow from OpenFoam [19], an open-source CFD software.

3.1.1. Selection of airfoils

In the selection of airfoils, consideration has been made with regards to surface roughness, which is responsible for premature boundary-layer transition and early turbulent separation which may lead to a significant reduction of the aerodynamic properties of the blades [20–23] and erosion of the leading edge [24].

Since contamination is unavoidable due to the exposure to insects, sand, dust, and rain, preference was given to the SG604X family of airfoils [25] with low sensitivity to surface roughness and contamination. These airfoils share a common geometric characteristic: an upper suction side with simple curvature and a lower pressure side with biconvex curvature, as shown in Fig. 4. The SG6040 airfoil is used at the root given its larger stiffness to support the bending moments, and the SG6042 and SG6043 are used at half the length and tip, respectively. For the sake of clarity, their lift and glide coefficients, C_L and C_G respectively, are presented in Appendix A.

3.1.2. Efficient aerodynamic configuration of the blade

Given the three main airfoils of the SG604X family, intermediate airfoils with unit chord are created by a linear transition at every 0.5 m along the span. The chord length C and the twist angle β at each section of the blade are determined following the Schmitz theory, see Appendix A. Fig. 5 depicts the chord length and twist angle distribution along the adimensional blade span. The resultant efficient configuration of the blade is illustrated in Fig. 6, which is the desired shape of the blade after deformation due to service loads.

3.1.3. CFD computational domain, boundary conditions and turbulence model

The problem of air flow around the rotor is assumed to be governed by the Navier–Stokes equations for incompressible viscous flow, and it was numerically solved using the Finite Volume Method (FVM) as implemented into the open-source software OpenFoam. A benchmark problem to validate the computational domain, boundary conditions and turbulence model is included in Appendix A.

Fig. 7 shows the adopted computational domain used to compute the aerodynamic forces. The model comprises the hub and the three blades rotating at 72 RPM, embedded in a large stationary domain with diameter 8R and length 12R, being R = 6.70 m the blade span length. The domain was discretized using an unstructured mesh of 6.268.947 nodes and 35.791.473 tetrahedral finite volume elements.

The boundary conditions are prescribed wind velocity at the inlet, and uniform atmospheric pressure in the lateral surface (open boundary) and in the outlet boundary. The surface of the blades is assumed to be a smooth no-slip wall. The assumed average environmental conditions are considered to be temperature $T = 28\ ^\circ C$, atmospheric pressure $P = 1.01325 \times 10^5$ Pa, constant density $\rho = 1.6808\ kg/m^3$, and kinematic viscosity $\nu = 1.45 \times 10^{-6}\ m^2/s$.

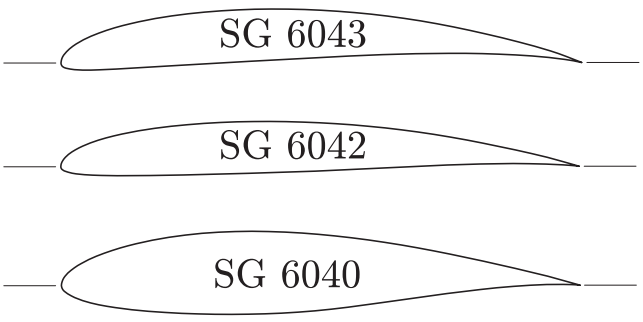

Fig. 4. The SG604X airfoil family.

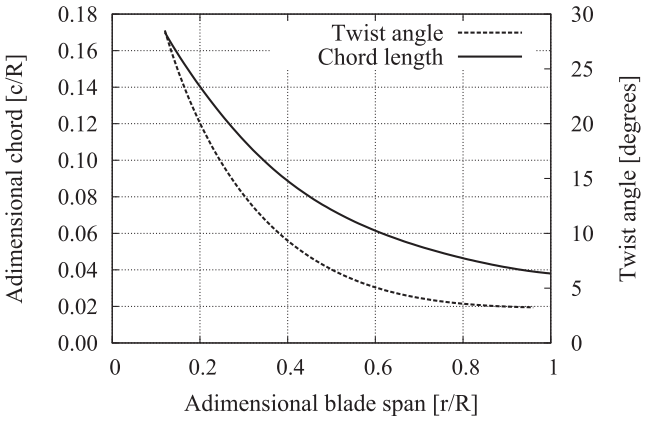

Fig. 5. Chord length and twist distribution of the blade.

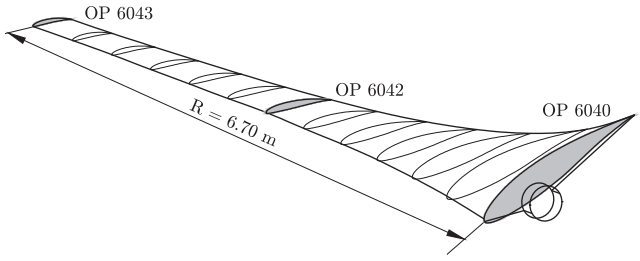

Fig. 6. Efficient aerodynamic configuration of the blade: desired shape after deformation due to service loads.

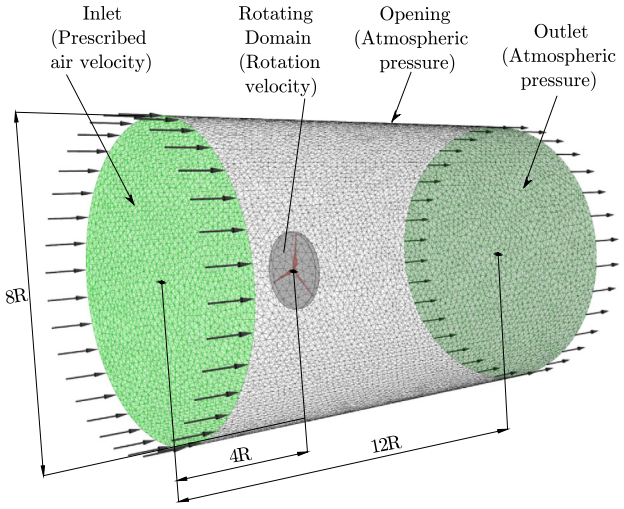

Fig. 7. The CFD computational domain. R is the blade span length.

3.1.4. CFD results: pressure gradients and aerodynamic forces over the blade

Fig. 8 depicts the air pressure over the surface of the blade.

The aerodynamic forces due to pressure gradients and viscous flow are depicted in Fig. 9. The performance curves for the wind turbine blades are presented Appendix A.

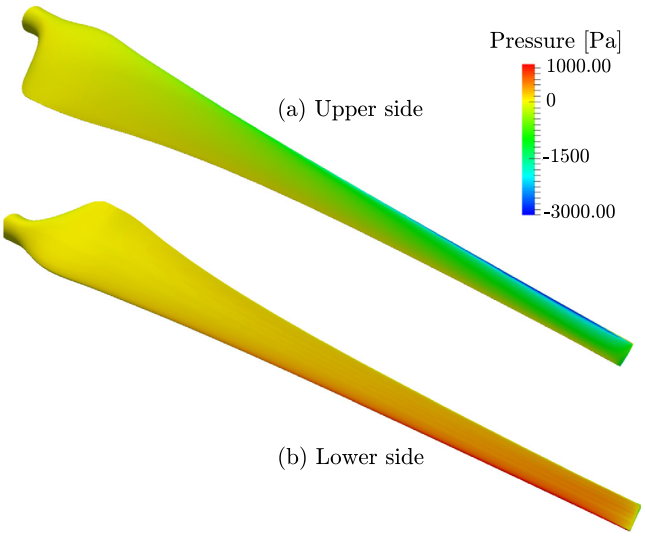

Fig. 8. Pressure over the blade: view from the upper side (a) and from the lower side (b).

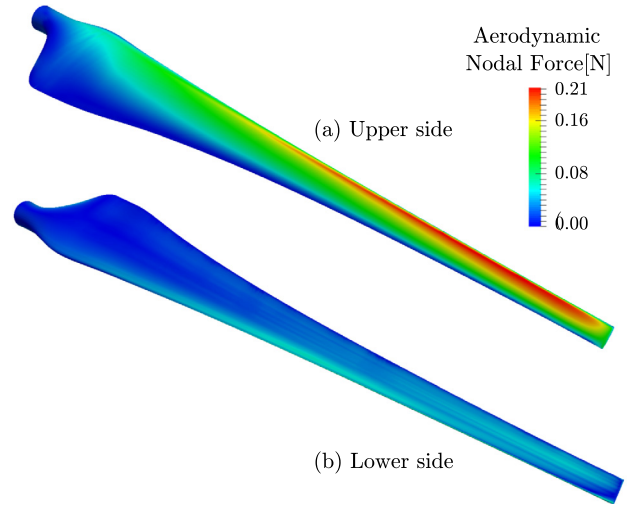

Fig. 9. Nodal aerodynamic forces on the blade: view from the upper side (a) and from the lower side (b).

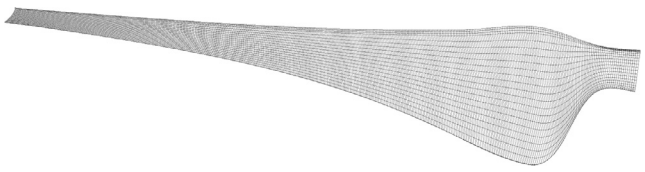

Fig. 10. Quadrilateral finite element mesh over the surface of the blade.

As mentioned before, there is no feedback or two-way interaction between the aerodynamic and the structural solvers. The one-way transferring of information from CFD results over unstructured meshes onto the structured IFEM shell discretization is achieved using the projection of resultant aerodynamic forces, see Section 3.3.

3.2. Finite element mesh of the blade surface

The structured quadrilateral mesh for the IFEM analysis consists of 22000 elements and 22044 nodes and presents refinement in curved areas of the blade. Fig. 10 depicts the mesh used in the two examples solved in this paper.

3.3. Transfer from CFD to IFEM

As mentioned before, the CFD analysis was performed over unstructured tetrahedral meshes while the IFEM analysis was performed over a structured quadrilateral mesh. In this approach, the areas of refinement on the CFD mesh, e.g. for capturing flow detachment, are most likely different than the areas of refinement on the structural mesh, i.e. for capturing high stress. Since the boundary of the CFD mesh that interfaces with the structural model is 2D, the one-way transferring of information from the aerodynamic model to the structure is easily achieved using the projection of resultant aerodynamic pressure onto the quadrilateral shell discretization, [26]. Other works, such as [27,28], successfully combined CFD results over unstructured meshes with finite element models with structured meshes using similar ideas.

3.4. Composite material configuration for the numerical applications

Two numerical examples with different material layout are solved in this work, considering reinforcement fabrics made of E-type glass fibers and an epoxy resin. Uniaxial fibers are oriented parallel to the longitudinal axis of the blade. Biaxial fabrics are woven at angles of 0° and 90°, and the 0° fibers are oriented parallel to the longitudinal axis of the blade. Double bias fibers are woven at angles of $+45^\circ$ and -45°, and is oriented at $+45^\circ$ from the longitudinal axis of the blade. The epoxy gelcoat is treated as an isotropic material. Table 1 presents the mechanical properties of these materials. Perfect bonding is assumed among the plies of the laminate, and ply waviness or deviation from the alignment direction [29] that could led to fiber failure is not considered.

The 2D version of the maximum stress failure criterion [30–32] is used in this work to verify the stresses in each layer of the blade. Failure will occur in the laminate if any of the normal or shear stresses in the local axes of a given layer, is equal to or exceeds the corresponding ultimate strengths of the layer. The laminate is considered to have failed if any of the following equations is violated:

$$\begin{aligned} -X_C < \sigma_1 < X_T \\ -Y_C < \sigma_2 < Y_T \\ -S < \tau_{12} < S \end{aligned} \tag{39}$$

Table 1
Mechanical properties of different E-type glass fibers, epoxy resin and gelcoat.

Mechanical property	Uniaxial	Biaxial	Double bias	Resin	Gelcoat
Elast. modul. E_1 [Pa]	70×10^9	70×10^9	30×10^9	5×10^9	5×10^9
Elast. modul. E_2 [Pa]	1×10^9	70×10^9	30×10^9	5×10^9	5×10^9
Density [Kg/m^3]	928.0	906.0	757.0	1150.0	650.0
Yield strength [Pa]	–	–	–	20×10^6	20×10^6
Poisson ratio	0.2	0.2	0.2	0.4	0.4
Thickness [mm]	0.50	0.50	0.35	–	0.25

where X_T is the ultimate longitudinal tensile strength, X_C is the ultimate longitudinal compresssive strength, Y_T is the ultimate transverse tensile strength, Y_C is the ultimate transverse compressive strength, and S is the ultimate shear strength. These values are given in [30,31] for E-type glass fibers and an epoxy resin.

3.4.1. Example 1: Multilayer laminate blade with a 7 step ply drop

The first numerical example is made of biaxial E-type glass fibers and an epoxy resin. A ply drop configuration similar to [33] is adopted, with a monotonic step drop from the root to the tip of the blade. As depicted in Fig. 11, the span was divided into seven regions. The number of plies in the root and the tip are eight and two, respectively.

The mechanical properties of the laminate formed by the biaxial fibers and epoxy were calculated following the rules of mixtures for composites using Halpin-Tsai equations [34,35], considering a volume fraction of 60%. Table 2 presents the resulting properties.

Fig. 12 depicts the stationary inertial forces, computed considering ply number, density, thickness, rotation velocity, and distance of each element to the rotation axis of the turbine. The IFEM solution i.e. the manufacturing shape of this blade is given in Section 4.2.

3.4.2. Example 2: multilayer laminate blade with a 10 step ply drop

This is a more realistic application that consists of a multilaminate blade using double bias, biaxial, and uniaxial fiber glass, and a layer of epoxy gelcoat with a ten step ply drop configuration, Fig. 13.

Table 3 presents the mechanical properties of the laminate calculated following the rules of mixtures for composites for a volume fraction of 60%.

The stationary inertial forces for example 2 are depicted in Fig. 14. The IFEM solution i.e. the manufacturing shape of this blade is given in Section 4.3.

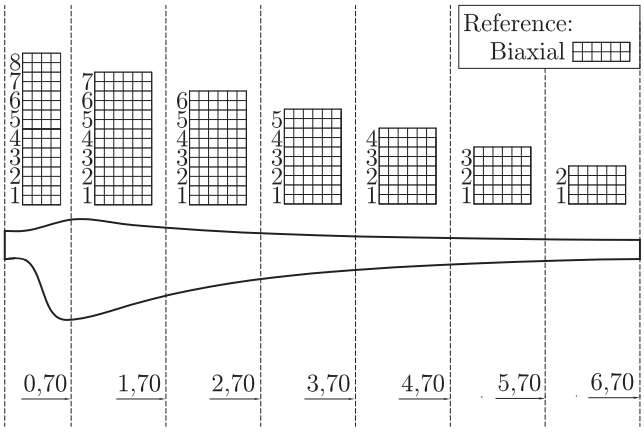

Fig. 11. Example 1: ply drop configuration of the blade.

Table 2
Example 1: mechanical properties of the laminate for a volume fraction of 60%.

Elasticity modulus $E_1 = E_2$ [Pa]	44.0×10^9
Shear modulus [Pa]	35.0×10^9
Tensile strength X_T [Pa]	1.06×10^9
Compressive strength X_C [Pa]	1.06×10^9
Tensile strength Y_T [Pa]	1.06×10^9
Compressive strength Y_C [Pa]	1.06×10^9
Shear strength S [Pa]	7.20×10^7
Density [kg/m^3]	1004.0
Poisson ratio	0.36
Thickness [mm]	0.50

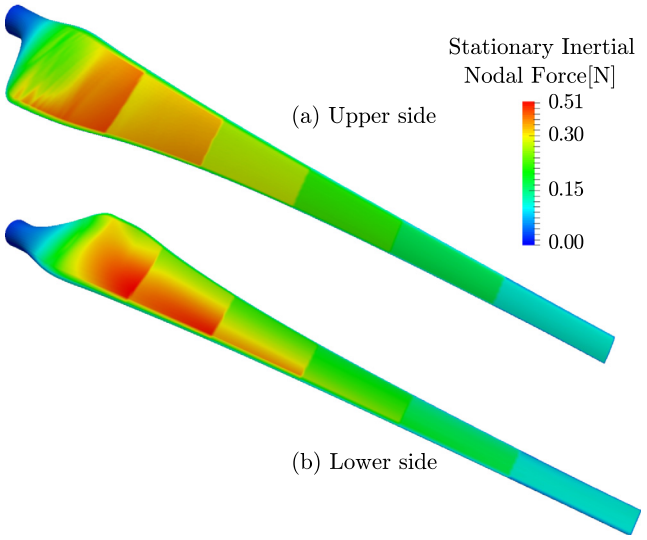

Fig. 12. Example 1: stationary inertial forces on the blade. View from the upper side (a) and from the lower side (b).

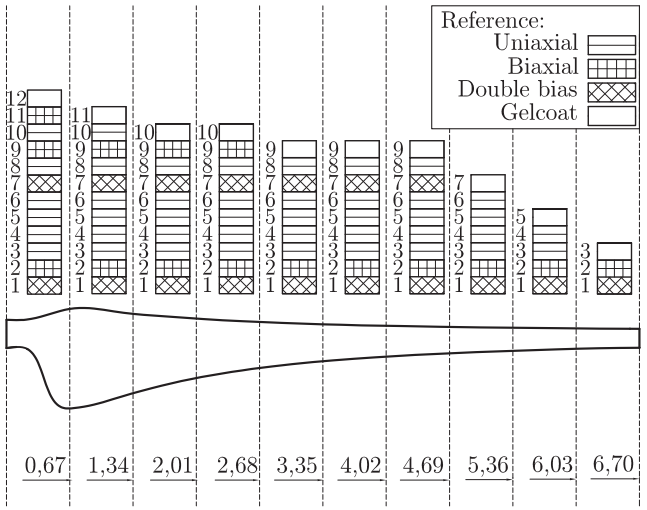

Fig. 13. Example 2: ply drop configuration of the blade.

Table 3
Example 2: mechanical properties of the different laminates for a volume fraction of 60%.

Mechan. propert.	Uniaxial	Biaxial	Double bias
Elast. mod. E_1 [Pa]	44.0×10^9	44.0×10^9	31.0×10^9
Elast. mod. E_2 [Pa]	12.6×10^9	44.0×10^9	24.7×10^9
Shear mod. [Pa]	16.5×10^9	35.0×10^9	15.0×10^9
Tensil. str. X_T [Pa]	1.06×10^9	1.06×10^9	9.20×10^8
Comp. str. X_C [Pa]	6.10×10^8	1.06×10^9	9.20×10^8
Tensil. str. Y_T [Pa]	3.10×10^7	1.06×10^9	9.20×10^8
Comp. str. Y_C [Pa]	1.18×10^8	1.06×10^9	9.20×10^8
Shear str. S [Pa]	7.20×10^7	7.20×10^7	6.35×10^7
Density [Kg/m^3]	1117.0	1004.0	914.0
Poisson ratio	0.36	0.36	0.36
Thickness [mm]	0.50	0.50	0.35

4. Numerical results

This sections presents the numerical examples computed with IFEM. First, a validation benchmark problem for multilayer shells is solved. Then, the manufacturing shape of the blades described

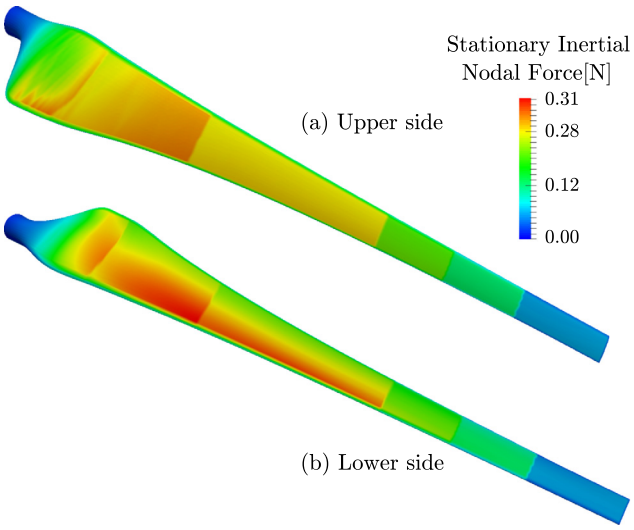

Fig. 14. Example 2: stationary inertial forces on the blade. View from the upper side (a) and the lower side (b).

in Sections 3.4.1 and 3.4.2 are computed and verified to ensure the feasibility of the IFEM solution.

4.1. Validation of the inverse shell model for multilayer shells

A benchmark problem for nonlinear shells with multilayered orthotropic materials is solved to demonstrate the shell IFEM accuracy. It consists of a cylinder with open ends that is pulled out by two opposite radial forces P, which has been considered by Masud et al. [36]. The cylinder has radius $R = 4.953$ m, length $L = 10.35$ m, and thickness $h = 0.094$ m, as illustrated in Fig. 15, and $P = 2.5e4$ N.

Due to the symmetry of the problem, only one-fourth of the cylinder is modeled using 18 elements along the axis, and 18 along the periphery.

The shell is made of two layers of composite material with Young moduli $E_1 = 30.5 \times 10^6$ Pa and $E_2 = 10.5 \times 10^6$ Pa, shear moduli $G_{12} = G_{13} = G_{23} = 4e6$ Pa, and Poisson ratii $\nu_{12} = \nu_{13} = \nu_{23} = 0.3125$. The composite is aligned such that $E_z = E_1$ and $E_\theta = E_2$ in the inner layer and $E_\theta = E_1$ and $E_z = E_2$ in the outer layer.

First, the deformed configuration of the cylinder is determined using "direct" FEM, Fig. 15(a). This solution matches the results of Masud et al. [36]. Afterward, the FEM-computed deformed mesh is adopted as the mesh for IFEM, as shown in Fig. 15(b). The loads are the pulling-out forces applied at the same nodes as those for FEM. As shown in Fig. 16, the IFEM solution is practically identical to the starting prescribed undeformed mesh given in Fig. 15(a).

4.2. IFEM Solution for Example 1

The manufacturing shape for the blade with a 7 step ply drop described in Section 3.4.1, was computed using only twelve iterations along two load steps, with a residue norm of 1×10^{-6}. This solution is depicted in Figs. 17 and 18.

4.2.1. Feasibility of the solution

1. *Inter-penetrated elements*: As depicted in Figs. 17 and 18, the current solution is free of such defects.
2. *Validity of the hypothesis of elasticity*: Table 4 summarizes the verification of the maximum stress criterion for example 1, and therefore the hypothesis of elasticity holds. The values of X_T, X_C, Y_T, Y_C and S are listed in Table 2.

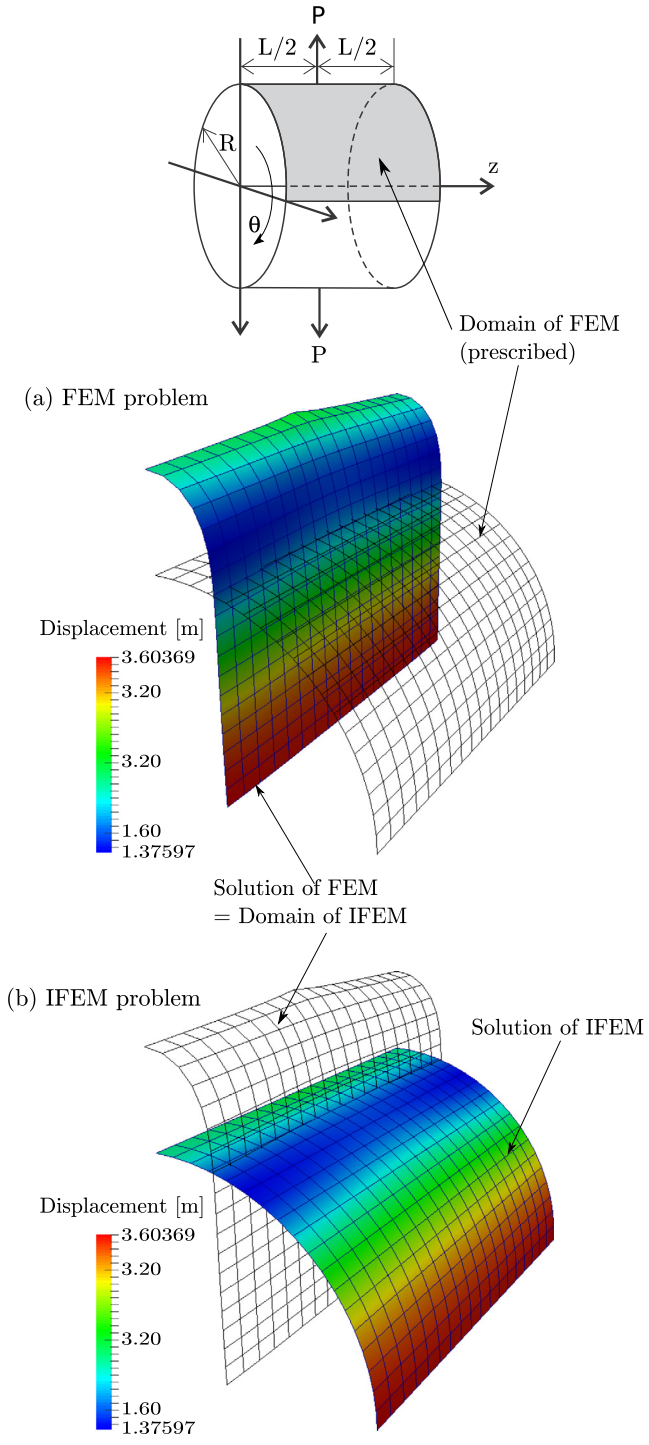

Fig. 15. Benchmark problem: pull out of a multilayered orthotropic cylinder. Direct FEM problem (a), and IFEM solution (b).

3. *Uniqueness of the solution*: the uniqueness is verified by the spectrum test.

Having succeeded at all these tests, the IFEM-computed undeformed configuration shown in Figs. 17 and 18 represents the manufacturing shape of the wind turbine blade of example 1. As a final verification, a FEM analysis has been performed to assess that the manufacturing shape of the blade recovers the aerodynamic optimal configuration under the service loads. Fig. 19 depicts the error in the nodal position of this analysis.

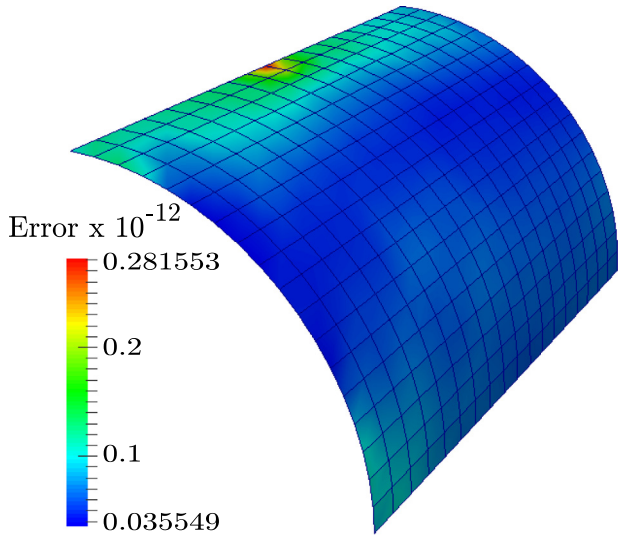

Fig. 16. Benchmark problem: error in the nodal positions in the undeformed configuration of the pullout cylinder computed with IFEM.

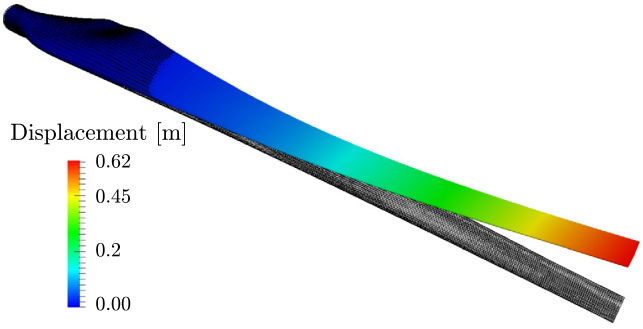

Fig. 17. Example 1: IFEM Solution. View from the leading edge. The prescribed aerodynamic geometry in wireframe, and manufacturing geometry in color surface.

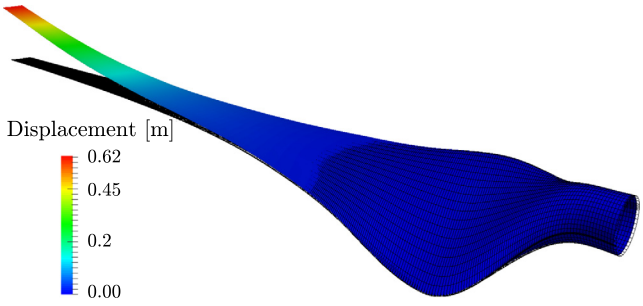

Fig. 18. Example 1: IFEM Solution. View from the trailing edge. The prescribed aerodynamic geometry in wireframe, and manufacturing geometry in the color surface.

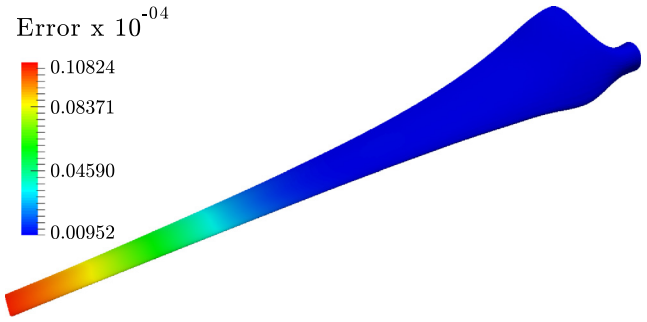

Fig. 19. Example 1: error in the nodal position of the FEM computed solution to verify that the manufacturing shape of the blade maps back to the aerodynamic optimal configuration.

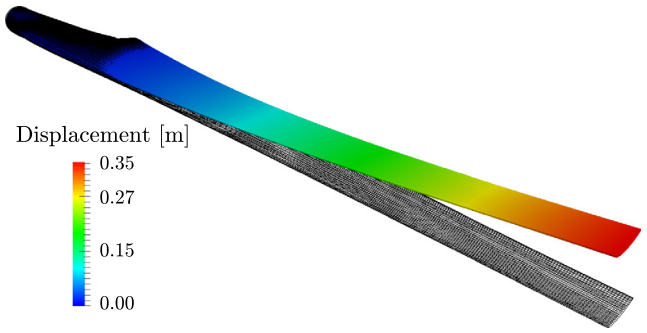

Fig. 20. Example 2: IFEM Solution. View from the leading edge. The prescribed aerodynamic geometry in wireframe, and manufacturing geometry in the color surface.

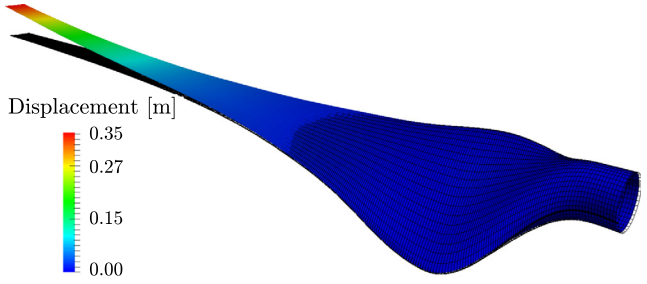

Fig. 21. Example 2: IFEM Solution. View from the trailing edge. The prescribed aerodynamic geometry in wireframe, and manufacturing geometry in color surface.

4.3. IFEM Solution for Example 2

The manufacturing shape for the laminate blade with a 10 step ply drop presented in Section 3.4.2, was computed using only fourteen iterations along two load steps, with a residue norm of 1×10^{-6}. This solution is depicted in Figs. 20 and 21.

Table 4
Example 1: verification of the maximum stress criterion. Stresses are measured in [Pa], and the values of X_T, X_C, Y_T, Y_C and S are listed in Table 2. Note that the 8th layer is made of gelcoat, and therefore the maximum stress criterion at that layer has not been considered.

Layer	max σ_1	min σ_1	max σ_2	min σ_2	max τ_{12}	min τ_{12}	$-X_C < \sigma_1 < X_T$
							$-Y_C < \sigma_2 < Y_T$
							$\lvert\tau_{12}\rvert <, S$
1	3.18×10^7	-2.27×10^7	3.40×10^7	-2.24×10^7	5.92×10^6	-4.43×10^6	ok
2	3.23×10^7	-2.31×10^7	1.91×10^7	-2.28×10^7	6.05×10^6	-4.38×10^6	ok
3	4.13×10^7	-2.36×10^7	1.19×10^7	-2.36×10^7	6.18×10^6	-4.95×10^6	ok
4	5.11×10^7	-2.41×10^7	6.68×10^6	-2.41×10^7	6.29×10^6	-4.35×10^6	ok
5	6.52×10^7	-2.21×10^7	7.88×10^6	-2.21×10^7	5.64×10^6	-4.31×10^6	ok
6	6.45×10^7	-2.28×10^7	1.12×10^7	-2.28×10^7	6.11×10^6	-4.28×10^6	ok
7	2.29×10^7	-3.01×10^7	1.63×10^7	-2.98×10^7	6.98×10^6	-4.30×10^6	ok

Table 5
Example 2: verification of the maximum stress criterion. Stresses are measured in [Pa], and the values of X_T, X_C, Y_T, Y_C and S are listed in Table 3. Note that layer 12 is made of gelcoat, and therefore the maximum stress criterion at that layer has not been considered.

Layer	max σ_1	min σ_1	max σ_2	min σ_2	max τ_{12}	min τ_{12}	$-X_C < \sigma_1 < X_T$
							$-Y_C < \sigma_2 < Y_T$
							$\lvert\tau_{12}\rvert < S$
1	2.16×10^7	-1.54×10^7	3.00×10^7	-1.54×10^7	2.01×10^7	-1.59×10^7	ok
2	2.62×10^7	-1.50×10^7	2.21×10^7	-1.49×10^7	1.62×10^7	-1.59×10^7	ok
3	2.27×10^7	-1.51×10^7	4.78×10^6	-1.51×10^7	2.07×10^6	-1.86×10^6	ok
4	3.09×10^7	-1.58×10^7	3.72×10^6	-1.58×10^7	2.12×10^6	-1.74×10^6	ok
5	3.93×10^7	-1.66×10^7	4.99×10^6	-1.66×10^7	2.47×10^6	-1.62×10^6	ok
6	4.80×10^7	-1.73×10^7	7.40×10^6	-1.73×10^7	2.99×10^6	-1.53×10^6	ok
7	4.39×10^7	-2.34×10^7	4.63×10^7	-2.34×10^7	1.79×10^7	-3.65×10^7	ok
8	6.25×10^7	-1.75×10^7	1.14×10^7	-1.75×10^7	4.22×10^6	-1.54×10^6	ok
9	2.85×10^7	-3.13×10^7	5.63×10^7	-3.13×10^7	3.82×10^7	-1.11×10^7	ok
10	1.43×10^7	-1.45×10^7	8.21×10^6	-1.45×10^7	2.56×10^6	-1.14×10^6	ok
11	1.43×10^7	-1.68×10^7	9.90×10^6	-1.68×10^7	1.55×10^6	-1.06×10^6	ok

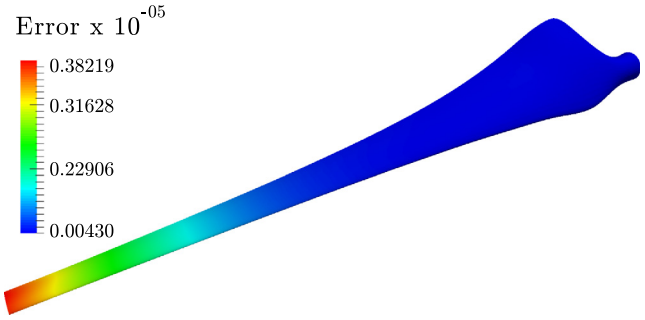

Fig. 22. Example 2: error in the nodal position of the FEM computed solution to verify that the manufacturing shape of the blade maps back to the aerodynamic optimal configuration.

4.3.1. Feasibility of the solution

1. *Inter-penetrated elements*: As depicted in Figs. 20 and 21, the solution for example 2 is free of such defects.
2. *Validity of the hypothesis of elasticity*: Table 5 summarizes the verification of the maximum stress criterion for example 2, and therefore the hypothesis of elasticity once again holds. The values of X_T, X_C, Y_T, Y_C and S are listed in Table 3.
3. *Uniqueness of the solution*: the uniqueness is verified by the spectrum test.

Since all test have succeeded, the IFEM-solution depicted in Figs. 20 and 21 represent the manufacturing shape of the wind turbine blade of example 2. Again, a FEM analysis has been performed to assess that the manufacturing shape of the blade recovers the aerodynamic optimal configuration under the service loads. Fig. 22 depicts the error in the nodal position of this analysis.

5. Conclusion

This work presents a novel methodology based on IFEM for nonlinear shells to design wind turbine blades made of composite materials, such that the blades attain an efficient prescribed aerodynamic shape after large elastic deformations. Compared to other multistep methods that compute the undeformed configuration of a body, IFEM is efficient from the computational point of view since it solves the nonlinear equilibrium equation only once.

The proposed IFEM formulation is capable of modeling multilayer orthotropic composite shells with high accuracy, as was shown in the benchmark problem. The capabilities and potentialities of the proposed approach are shown through two numerical examples with different composite multilayer materials and ply-drops along the blade span.

Future work will consist in the implementation of optimization techniques to automatically determine the stacking sequence, ply drop configuration and fiber orientation of the composite materials used to manufacture the blades.

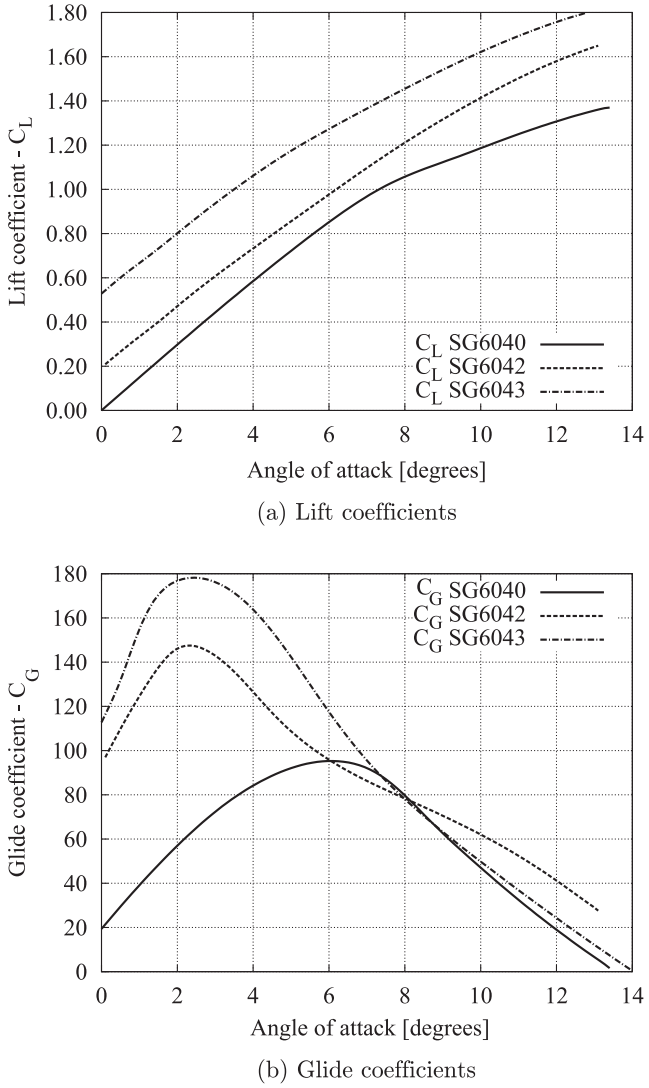

Fig. 23. Lift (a) and glide (b) coefficients for the SG604X airfoil family.

Acknowledgments

The authors gratefully acknowledge the financial support from CONICET (Argentine Council for Scientific and Technical Research). A.E. Albanesi also acknowledges the National Technological University of Argentina (UTN) for the Grant PID ENUTNFE0002146.

Appendix A. Aerodynamic analysis data

A.1. Lift and glide coefficients of the airfoils

The lift and glide coefficients, C_L and C_G respectively, of the SG604X family or airfoils are shown in Fig. 23.

A.2. Chord length and twist angle determined by Schmitz theory

The chord length C and the twist angle β for intermediate airfois are determined following the Schmitz theory [37–39]:

$$C(r) = \frac{16\ \pi\ r}{B\ C_L} \sin^2\left(\frac{1}{3}\arctan\frac{R}{\lambda\ r}\right) \tag{40}$$

$$\beta(r) = \frac{2}{3}\arctan\left(\frac{R}{\lambda\ r}\right) - \alpha_D \tag{41}$$

where r⩽R is the distance between the considered section and the rotation axis of the turbine, R is the turbine radius, B is the number of blades, λ is the tip speed ratio and α_D is the angle of attack at the prescribed operation conditions.

A.3. Wind turbine performance curves

All of the CFD calculation have been performed with a residue norm of 1×10^{-5}, and demanded between 600 and 800 iterations each. The performance curves were calculated sweeping through wind velocities in a series of steady state simulations, all with a rotational speed of 72 RPM. A total of 35 simulations were performed, considering wind velocities V of 2, 4, 6, 8, 10, 12 y 14 m/s.

The power P delivered by the rotor is measured in W, and is computed as

$$P = \boldsymbol{\tau} \cdot \boldsymbol{\omega}, \tag{42}$$

where $\boldsymbol{\tau}$ is the torque generated by the blades measured in Nm, and $\boldsymbol{\omega}$ is the angular velocity measured in radians per second. The ratio of the power delivered by the rotor to the power available in the wind for the same cross section A, results in the aerodynamic efficiency of the blades

$$\eta_A = \frac{P}{\frac{1}{2}\rho A V^3}. \tag{43}$$

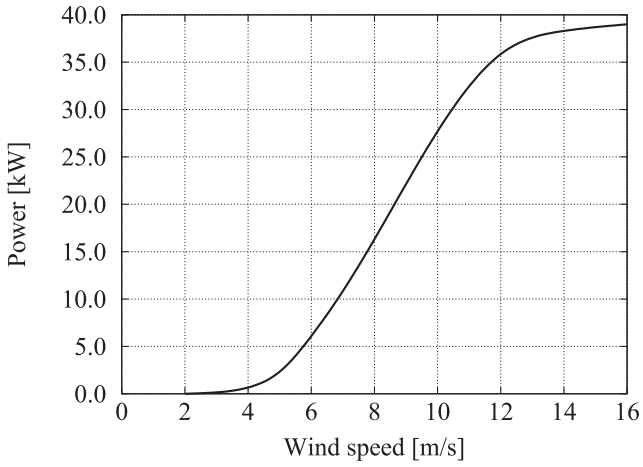

(a) Power vs. wind velocity

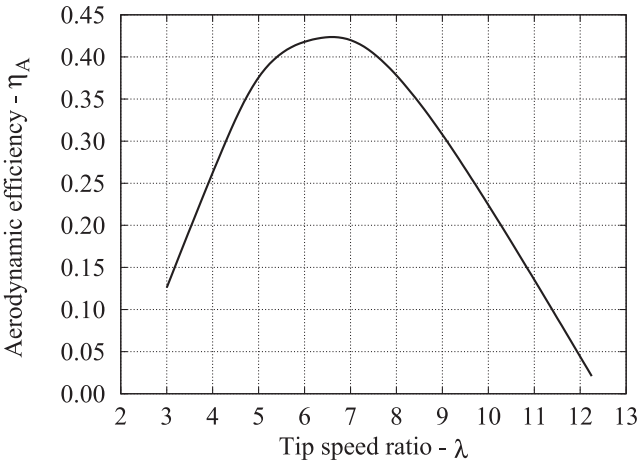

(b) Efficiency vs. tip speed ratio

Fig. 24. Power curve (a) and aerodynamic efficiency (b) of the blade.

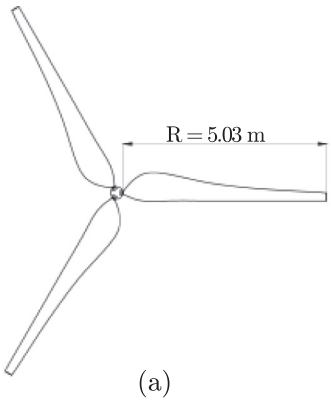

(a)

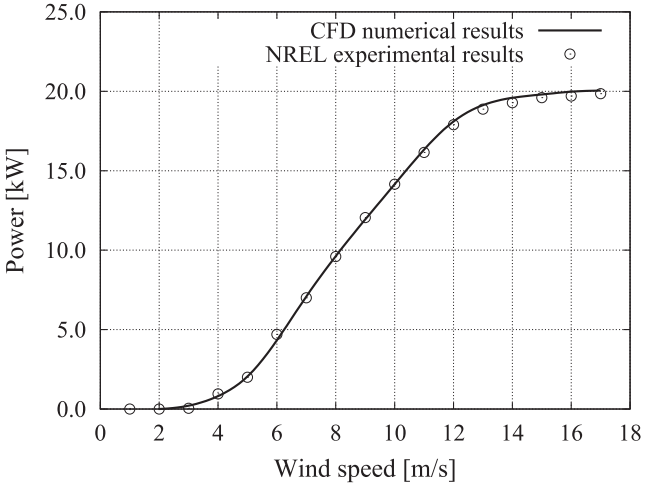

(b)

Fig. 25. Validation of CFD results: NREL CER wind turbine (a), and the comparison between CFD results with NREL experimental results (b).

The turbine delivers 12 kW at the prescribed condition with an aerodynamic efficiency of 42%. Fig. 24 depicts the power versus wind velocity curve and efficiency versus λ curve.

A.4. Validation of CFD model and procedure

The CFD model, turbulence model, mesh refinement and computation procedure were validated with the 20 kW NREL Combined Experimental Rotor (NREL CER), a three-bladed rotor with a span of 5.03 m and non-linear twist distribution, [40], Fig. 25 (a). It was selected because of the similarity in blade length and twist distribution.

The computational domain for the NREL CER had the same relative dimensions to that of Fig. 7 (given that R = 5.03 m), and following [40], the pitch angle was set to 5° degrees and the rotational velocity was set to 72 rpm (RPM). An unstructured mesh of 35.822.607 tetrahedral elements was created following the procedure described in Section 3.1.3, and the steady-state solver for incompressible and turbulent flow *simpleFoam* with the k-SST turbulence model and the MRF approach has been used.

Validation results are presented in Fig. 25(b), where the numerical results computed with CFD are in excellent agreement with NREL experimental results of [40], demonstrating that the computational domain, turbulence model, and mesh refinement are correctly chosen and configured.

References

[1] World Energy Scenarios. Composing Energy Futures to 2050. London: World Energy Council; 2013.
[2] Shokrieh MM, Rafiee R. Fatigue life prediction of wind turbine rotor blades manufactured from composites. In: Vassilopoulos AP, editor. Fatigue Life Prediction of Composites and Composite Structures. Woodhead Publishing Series in Composites Science and Engineering. Woodhead Publishing; 2010. p. 505–37. chapter 14.
[3] Amaro AM, Reis PNB, Neto MA, Louro C. Effect of different commercial oils on mechanical properties of composite materials. Compos Struct 2014;118:1–8.
[4] Sookay NK, von Klemperer CJ, Verijenko VE. Environmental testing of advanced epoxy composites. Compos Struct 2003;62(3–4):429–33.
[5] Abdel-Magid B, Ziaee S, Gass K, Schneider M. The combined effects of load moisture and temperature on the properties of E-glass/epoxy composites. Compos Struct 2005;71(3–4):320–6. Fifth International Conference on Composite Science and Technology (ICCST).
[6] Bazilevs Y, Hsu M-C, Kiendl J, Benson DJ. A computational procedure for prebending of wind turbine blades. Int J Numer Meth Eng 2012;89(3):323–36.
[7] Kiendl J, Bletzinger K-U, Linhard J, Wüchner R. Isogeometric shell analysis with kirchhoff–love elements. Comput Methods Appl Mech Eng 2009;198:3902–14.
[8] Chen X, Zheng C, Xu W, Zhou K. An asymptotic numerical method for inverse elastic shape design. ACM Trans Graph 2014;33(4, Article 95):1–11.
[9] Fachinotti V, Cardona A, Jetteur Ph. Finite element modelling of inverse design problems in large deformations anisotropic hyperelasticity. Int J Numer Meth Eng 2008;74:894–910.
[10] Albanesi AE, Fachinotti VD, Cardona A. Inverse finite element method for large-displacement beams. Int J Numer Meth Eng 2010;84:1166–82.
[11] Fachinoti VD, Albanesi AE, Martínez Valle JM. Inverse finite element modeling of shells using the degenerate solid approach. Comput Struct 2015;157:89–98.
[12] Dvorkin EN, Bathe K-J. A continuum mechanics based four-node shell element for general nonlinear analysis. Eng Comput 1984;1:77–88.
[13] Bucalem ML, Bathe K-J. The mechanics of solids and structures. Hierarchical modeling and the finite element solution. In: Computational Fluid and Solid Mechanics. Springer-Verlag; 2011.
[14] Simo JC, Fox DD, Rifai MS. On a stress resultant geometrically exact shell model. Part III: Computational aspects of the nonlinear theory. Comput Methods Appl Mech Eng 1990;79:21–70.
[15] Albanesi AE, Pucheta MA, Fachinotti VD. A new method to design compliant mechanisms based on the inverse beam finite element model. Mech Mach Theory 2013;65:14–28.
[16] Albanesi AE. Inverse design methods for compliant mechanisms. Santa Fe, Argentina: Faculty of Engineering and Water Sciences, National Littoral University; 2011 (Ph.D. thesis).
[17] Golub GH, Van Loan CF. Matrix Computations. 3rd ed. Baltimore: Johns Hopkins University Press; 1996.
[18] Allgoewer EL, Georg K. Introduction to numerical continuation methods. Society for Industrial and Applied Mathematics (SIAM); 2003.
[19] Openfoam: Open source field operation and manipulation; 2015. URL: www.openfoam.com.
[20] Sareen A, Sapre CA, Selig MS. Effects of leading edge erosion on wind turbine blade performance. Wind Energy 2014;17:1531–42.
[21] Ren N, Ou J. Dust effect on the performance of wind turbine airfoils. J Electromagn Anal Appl 2009;1:102–7.
[22] Freudenreich K, Kaiser K, Schaffarczyk AP, Winkler H, Stahl B. Reynolds number and roughness effects on thick airfoils for wind turbines. Wind Eng 2004;28(5):529–46.
[23] Van Rooij RM, Timmer WA. Roughness sensitivity considerations for thick rotor blade airfoils. ASME J Sol Energy Eng 2003;125(4):468–78.
[24] Golfman Y. Hybrid Anisotropic Materials for Wind Power Turbine Blades. CRC Press; 2012.
[25] Giguére PP, Selig MS. New airfoils for small horizontal axis wind turbines. ASME J Sol Energy Eng 1998;120(2):108–14.
[26] Hou G, Wang J, Layton A. Numerical methods for fluid-structure interaction – a review. Commun Comput Phys 2012;12(2):337–77.
[27] Yu DO, Kwon OJ. Predicting wind turbine blade loads and aeroelastic response using a coupled CFD-CSD method. Renewable Energy 2014;70:184–96.
[28] Yu DO, Kwon OJ. Time-accurate aeroelastic simulations of a wind turbine in yaw and shear using a coupled CFD-CSD method. J Phys: Conf Ser 2014;524.
[29] Altmann A, Gesell P, Drechsler K. Strength prediction of ply waviness in composite materials considering matrix dominated effects. Compos Struct 2015;127:51–9.
[30] Barbero EJ. Introduction to Composite Materials Design. 2nd ed. CRC Press; 2011.
[31] Kaw AK. Mechanics of Composite Materials. 2nd ed. CRC Press; 2006.
[32] Jones R. Mechanics of Composite Materials. 2nd ed. Taylor and Francis; 1999.
[33] Bir G, Migliore P. Preliminary structural design of composite blades for two- and three-bladed rotors. National Renewable Energy Laboratory (NREL) Report NREL/TP-500-31486; 2004. p. 1–37.
[34] Reddy JN, Miravete A. Practical Analysis of Composite Laminates. CRC Press; 1995.
[35] Hollmann M. Composite Aircraft Design. Aircraft Designs Incorporated; 1988.
[36] Masud A, Tham LC, Liu KW. A stabilized 3-d co-rotational formulation for geometrically nonlinear analysis of multi-layered composite shells. Comput Mech 2000;26(1):1–12.
[37] Gasch R, Twele J. Blade Geometry According to Betz and Schmitz. Berlin Heidelberg: Springer; 2012.
[38] McCosker J. Design and Optimization of Small Wind Turbines. Connecticut. USA: Rensselaer Polytechnic Institute; 2012 (Master thesis).
[39] Gundtoft S. Wind turbines. University College of Aarhus; 2009.
[40] Giguere P, Selig MS. Design of a tapered and twisted blade for the nrel combined experiment rotor. March 1998–March 1999. National Renewable Energy Laboratory (NREL) Report NREL/SR-500-26173; 1999. p. 1–32.